INTERNATIONAL JOURNAL FOR NUMERICAL METHODS IN FLUIDS, VOL. 14, 505–527 (1992)

CELL VERTEX FINITE VOLUME DISCRETIZATIONS IN THREE DIMENSIONS

P. I. CRUMPTON AND G. J. SHAW

Oxford University Computing Laboratory, 11 Keble Road, Oxford, OX1 3QD, U.K.

SUMMARY

The cell vertex method is generalized to three dimensions. It is proved that there exists a one-parameter family of eight-point three-dimensional methods with second-order truncation error on parallelepipeds. Using different triangulations of control volume faces, various finite volume methods are derived. Some of these are identified as members of the aforementioned one-parameter family and may be regarded as second-order upwind schemes. A Fourier analysis is used to investigate the spectral properties of these discretizations.

Numerical experiments illustrate that second-order global accuracy is achieved on parallelepiped grids, as suggested by the theory. Randomly perturbed, stretched, sheared meshes are used to test these methods to destruction. It is found that upwinding improves both the accuracy on distorted meshes and the spectrum of the discretization.

KEY WORDS Cell vertex Accuracy on parallelepipeds Triangulated control volumes

1. INTRODUCTION

The true nature of fluid flows past complex geometries can only be adequately represented by three-dimensional systems of partial differential equations. Because the size of the resulting algebraic systems can easily exhaust the memory of the largest computers, mesh refinement may be impractical and the accuracy of the underlying discretization is paramount. In addition, direct solvers for these systems are computationally infeasible and iterative techniques must be employed. The convergence of these methods depends critically on the spectral properties of the underlying discretization.

Cell vertex finite volume methods are becoming increasingly popular in applications to the Euler and Navier–Stokes equations in two dimensions. This is largely due to the experimental and theoretical evidence that such methods are significantly more accurate on non-uniform meshes than their cell-centred counterparts.[1–3]

This paper generalizes the cell vertex method to three dimensions. The resulting methods are applied to scalar conservation laws for which their accuracy and spectral properties are examined, as a first step towards the treatment of non-linear hyperbolic systems. The paper begins with a brief review of the analysis of the one- and two-dimensional methods. By using different integration rules over the faces of hexahedral control volumes, various eight-point three-dimensional generalizations are derived. These are identified as members of a one-parameter family of cell vertex methods which have second-order truncation errors on parallelepiped meshes. Some

0271–2091/92/050505–23$11.50

Received November 1990
Revised June 1991

members of this family are shown to have more desirable spectral properties than others, although all admit spurious oscillatory solution modes.

The global accuracy of these methods on non-uniform meshes is both confirmed and compared through numerical experiments with linear advection. Finally, by imposing a helical flow field, an upwind cell vertex discretization is introduced and shown to possess second-order accuracy.

2. THE CELL VERTEX DISCRETIZATION IN ONE AND TWO DIMENSIONS

Since this paper is concerned with the accurate discretization of spatial derivative terms, the following discussion is directed at systems of steady state conservation laws. However, its conclusions are equally applicable to time-dependent problems.

Consider the steady conservation law

$$\nabla \cdot \mathbf{F} = 0, \tag{1}$$

where $\mathbf{F}$ is a function of the solution q in one, two or three dimensions. The basic philosophy of the cell vertex finite volume method is to:

(i) split the domain into non-overlapping convex control volumes;
(ii) store approximate solutions at the vertices of these control volumes;
(iii) integrate the equation over a typical control volume Γ and apply the divergence theorem,

$$\int_\Gamma \nabla \cdot \mathbf{F} \mathrm{d}v = \oint_{\partial\Gamma} \mathbf{F} \cdot \mathbf{n} \mathrm{d}s, \tag{2}$$

where $\mathbf{n}$ is a unit normal to Γ; a cell residual R is defined to be

$$R = \frac{1}{V} \oint_{\partial\Gamma} \mathbf{F} \cdot \mathbf{n} \mathrm{d}s \tag{3}$$

where V is the volume of the cell Γ; by (2), setting $R=0$ corresponds to solving (1) as $V \to 0$

(iv) approximate R using some numerical integration rule around the control volume, thus giving a cell-based equation in terms of node-based unknowns;
(v) set each individual cell residual to zero whilst imposing relevant boundary conditions.

This produces a compact, conservative and accurate stencil, ideal for systems of conservation laws.

In one dimension for linear advection

$$aq_x = 0, \tag{4}$$

for which $F(q)=aq$, the cell residual R is approximated over a two-point control volume as

$$R \approx \frac{a(q_{i+1} - q_i)}{x_{i+1} - x_i}, \tag{5}$$

where $\{x_i\}_{i=1}^N$ is a mesh with nodes $x_i < x_{i+1}$ bounding the control volumes and $q_i \approx q(x_i)$. Let the discrete system of cell residuals and boundary conditions be written

$$L\mathbf{q} = \mathbf{f}.$$

Denoting the vector of truncation errors by $\boldsymbol{\tau}$ and the global error by $\mathbf{e}$,

$$L\mathbf{e} = \boldsymbol{\tau}.$$

Thus

$$\|\mathbf{e}\| \leqslant \|L^{-1}\| \, \|\boldsymbol{\tau}\|.$$

Given that the matrix L is stable, $\|L^{-1}\| \leqslant c$ for some constant c, the global error is of the same order as the truncation error and the sharpest bound is obtained by minimizing $\boldsymbol{\tau}$. This is achieved when $\boldsymbol{\tau}$ is evaluated at the centre of the cell. It should be noted that if equation (4) included source terms, these should be evaluated at the same point as the truncation error. One of the paramount issues of this argument is the correct choice of norm. This is not addressed here; for a detailed discussion see Reference 4.

It is trivial to show that equation (5) is the unique cell vertex discretization with second-order truncation error at the centre of the cell. The Fourier symbol for this stencil is

$$S(\theta) = 2i \frac{a}{h} \sin\left(\frac{\theta}{2}\right), \qquad \theta \in (-\pi, \pi],$$

for a uniform mesh with mesh spacing h. Since $S(\theta)$ vanishes only for $\theta = 0$, this discretization admits no spurious oscillatory modes. A detailed description of the Fourier symbol is given in Section 3.1. Hence in one dimension the cell vertex method with second-order truncation error is unique, compact, conservative, admits no spurious oscillatory modes and suffers no loss of accuracy due to mesh distortion.

In two dimensions the cell vertex method has been extensively applied to convex quadrilateral control volumes. In general, for a second-order truncation error the first six terms of the Taylor series need to be set to zero. Hence for a four-point stencil this accuracy is only achieved for quadrilaterals with special properties, such as parallelograms. The following existence and uniqueness theorem characterizes two-dimensional cell vertex methods for linear advection

$$aq_x + bq_y = 0, \tag{6}$$

for which $\mathbf{F}(q) = (aq, bq)^{\mathrm{T}}$.

Theorem 1

There exists a unique four-point cell vertex method for linear advection in two dimensions with second-order truncation error on parallelograms. It has the following properties:

1. opposite coefficients of the stencil sum to zero;
2. the stencil admits a spurious oscillatory solution mode.

Proof. Let the four-point discretization be written

$$\mathbf{a} \cdot \nabla q \approx \sum_{i=1}^{4} \alpha_i q_i,$$

where $\boldsymbol{a} = (a, b)^{\mathrm{T}}$ is constant, $\{\alpha_i\}_{i=1}^{4}$ are the stencil coefficients ordered as in Figure 1, $q_i \approx q(\mathbf{x}_i)$ is an approximate solution at the vertices $\mathbf{x}_i$ and the centre of the parallelogram, $\mathbf{x}_0$, is defined as the average of these vertices. Expanding the first six terms in a Taylor series about $\mathbf{x}_0$ gives

$$\boldsymbol{a} \cdot \nabla q(\mathbf{x}_0) \approx \sum_{i=1}^{4} \alpha_i (q|_{\mathbf{x}=\mathbf{x}_0} + \delta x_i q_x|_{\mathbf{x}=\mathbf{x}_0} + \delta y_i q_y|_{\mathbf{x}=\mathbf{x}_0} + \delta x_i \delta y_i q_{xy}|_{\mathbf{x}=\mathbf{x}_0} + \frac{\delta x_i^2}{2} q_{xx}|_{\mathbf{x}=\mathbf{x}_0} + \frac{\delta y_i^2}{2} q_{yy}|_{\mathbf{x}=\mathbf{x}_0}), \tag{7}$$

where $\delta \mathbf{x}_i = (\delta x_i, \delta y_i)^{\mathrm{T}} = \mathbf{x}_i - \mathbf{x}_0$. Let

$$\mathbf{l} = (1, 1)^{\mathrm{T}}, \qquad \mathbf{A} = \begin{pmatrix} \delta x_1 & \delta x_2 \\ \delta y_1 & \delta y_2 \end{pmatrix}, \qquad \mathbf{b} = (\delta x_1 \delta y_1 \;\; \delta x_2 \delta y_2)^{\mathrm{T}}, \qquad \mathbf{C} = \begin{pmatrix} (\delta x_1)^2 & (\delta x_2)^2 \\ (\delta y_1)^2 & (\delta y_2)^2 \end{pmatrix}.$$

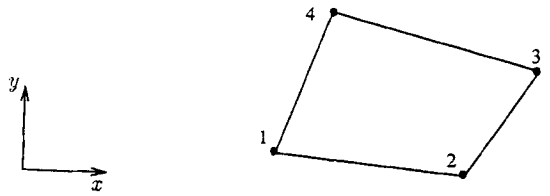

Figure 1. Ordering of the nodes for a two-dimensional control volume

Note that on a parallelogram

$$\delta \mathbf{x}_i = -\delta \mathbf{x}_{i+2}, \qquad i = 1, 2.$$

Assuming $\boldsymbol{a} \cdot \nabla q = 0$ in equation (7), a second-order truncation error is achieved provided that

$$\begin{pmatrix} \mathbf{l}^{\mathrm{T}} & \mathbf{l}^{\mathrm{T}} \\ A & -A \\ \mathbf{b}^{\mathrm{T}} & \mathbf{b}^{\mathrm{T}} \\ C & C \end{pmatrix} \begin{pmatrix} \alpha_1 \\ \vdots \\ \alpha_4 \end{pmatrix} = \begin{pmatrix} 0 \\ \boldsymbol{a} \\ 0 \\ 0 \end{pmatrix},$$

where $\mathbf{0} = (0, 0)^{\mathrm{T}}$. Introducing alternative variables

$$\beta_i = \alpha_i + \alpha_{i+2} \quad \text{and} \quad \gamma_i = \alpha_i - \alpha_{i+2}, \qquad i = 1, 2, \tag{8}$$

results in

$$\begin{pmatrix} \mathbf{0}^{\mathrm{T}} & \mathbf{l}^{\mathrm{T}} \\ A & 0 \\ \mathbf{0}^{\mathrm{T}} & \mathbf{b}^{\mathrm{T}} \\ 0 & C \end{pmatrix} \begin{pmatrix} \boldsymbol{\gamma} \\ \boldsymbol{\beta} \end{pmatrix} = \begin{pmatrix} 0 \\ \boldsymbol{a} \\ 0 \\ \mathbf{0} \end{pmatrix},$$

where $\boldsymbol{\beta} = (\beta_1, \beta_2)^{\mathrm{T}}$ and $\boldsymbol{\gamma} = (\gamma_1, \gamma_2)^{\mathrm{T}}$. Hence we require

$$\mathbf{A}\boldsymbol{\gamma} = \boldsymbol{a} \tag{9}$$

and

$$\begin{pmatrix} \mathbf{l}^{\mathrm{T}} \\ \mathbf{b}^{\mathrm{T}} \\ C \end{pmatrix} \boldsymbol{\beta} = \begin{pmatrix} 0 \\ \vdots \\ 0 \end{pmatrix}. \tag{10}$$

The system (9) has a unique solution $\boldsymbol{\gamma}$ for non-trivial parallelograms since $\det(\mathbf{A}) = V/2$, where V is the volume of the parallelogram. The determinant of the first two rows of the matrix $(\mathbf{l}^{\mathrm{T}}, \mathbf{b}^{\mathrm{T}}, C)^{\mathrm{T}}$ is

$$d = \delta x_2 \delta y_2 - \delta x_1 \delta y_1. \tag{11}$$

Without loss of generality the parallelogram may be oriented such that $\delta y_1 = \delta y_2$ and thus $d = V/2$. Hence $(\mathbf{l}^{\mathrm{T}}, \mathbf{b}^{\mathrm{T}}, C)^{\mathrm{T}}$ is of rank two and $\boldsymbol{\beta} = \mathbf{0}$ is the unique solution of (10). This proves existence and uniqueness and property 1 follows immediately from (8).

Property 2 is proved by seeking solutions of the homogeneous equations of the form

$$q_{ij} = \Theta_1^i \, \Theta_2^j,$$

where q_{ij} is defined on some regular parallelogram (i, j) mesh. Substituting this into the stencil gives

$$\alpha_1(1-\Theta_1\Theta_2)+\alpha_2(\Theta_1-\Theta_2)=0. \tag{12}$$

This has the solution $\Theta=(1, 1)^T$, $(-1, -1)^T$. The first of these solutions is the consistency condition whilst the second represents a high-frequency oscillatory solution mode. □

Through a finite volume formulation a cell vertex stencil may be derived as follows. In two dimensions $\mathbf{n}=(dy, -dx)^T$ and hence from (3)

$$R=\frac{1}{V}\oint_{\partial\Gamma}(aq\,dy-bq\,dx).$$

Approximating the line integral by the trapezium rule gives the four-point stencil

$$R=\frac{1}{V}\{[a(x_2-x_4)-b(y_2-y_4)](q_1-q_3)+[a(x_3-x_1)-b(y_3-y_1)](q_2-q_4)\}. \tag{13}$$

This reduces to the unique method of the theorem for control volumes which are parallelograms. Much analysis has been performed on this discretization.[1-4] In Reference 1 the cell vertex method is shown to maintain its order of accuracy under mesh stretching, unlike its cell-centred counterpart. In Reference 4 global second-order accuracy is proved and demonstrated if the points bisecting the diagonals of the quadrilateral control volume differ by less than $O(h)$.

The Fourier symbol[2] of this stencil on a uniform mesh is given by

$$S(\theta)=i\frac{a+b}{h}\sin\left(\frac{\theta_1+\theta_2}{2}\right)+i\frac{a-b}{h}\sin\left(\frac{\theta_1-\theta_2}{2}\right),$$

where $\theta=(\theta_1, \theta_2)^T\in(-\pi, \pi]^2$. This symbol vanishes in the case

$$\theta=(\pi, \pi)^T.$$

This represents a spurious oscillatory chequerboard mode which is undetected by the discretization. In addition, there is a characteristic mode where $S(\theta)=0$ which is normal to $(a, b)^T$ in the neighbourhood of the origin. These modes severely inhibit the convergence of any iterative solver; for further details see Reference 5. In summary, the method has a compact, conservative four-point stencil and is accurate on regular quadrilaterals. However, the Fourier symbol admits spurious oscillatory modes.

3. CELL VERTEX DISCRETIZATIONS IN THREE DIMENSIONS

In this paper eight-point cell vertex methods for three-dimensional conservation laws are examined. Consider the equation

$$\nabla\cdot\mathbf{F}=F_x+G_y+H_z=0,$$

where $\mathbf{F}=\mathbf{F}(q)$ and $q=q(\mathbf{x})$ with $\mathbf{x}=(x, y, z)^T$. From equation (3)

$$R=\frac{1}{V}\oint_{\partial\Gamma}\mathbf{F}\cdot\mathbf{n}\,ds,$$

where V is the volume of Γ. Consider a general hexahedral volume with planar faces as in Figure 2. On the face 1678

$$\mathbf{n}ds=\tfrac{1}{2}\,\delta\mathbf{x}_{67}\wedge\delta\mathbf{x}_{18},$$

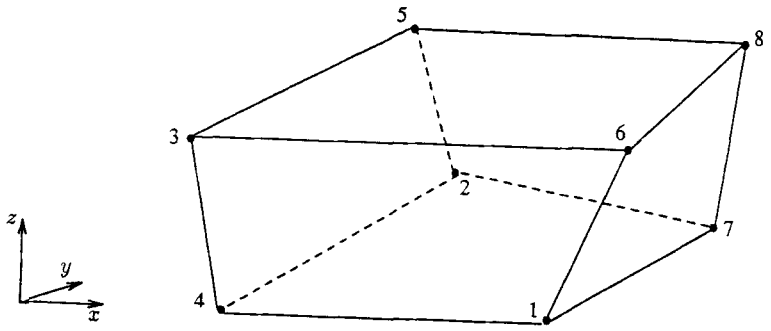

Figure 2. A general eight-point volume

where $\delta\mathbf{x}_{ij}=\mathbf{x}_i-\mathbf{x}_j$. Hence, using the midpoint rule to approximate the surface integral of (3), the cell residual is defined as

$$R\approx\frac{1}{V}[\tfrac{1}{4}(\mathbf{F}_2+\mathbf{F}_3+\mathbf{F}_4+\mathbf{F}_5)\cdot\tfrac{1}{2}\delta\mathbf{x}_{54}\wedge\delta\mathbf{x}_{23}+\tfrac{1}{4}(\mathbf{F}_1+\mathbf{F}_3+\mathbf{F}_4+\mathbf{F}_6)\cdot\tfrac{1}{2}\delta\mathbf{x}_{64}\cdot\delta\mathbf{x}_{31}$$
$$+\tfrac{1}{4}(\mathbf{F}_1+\mathbf{F}_2+\mathbf{F}_4+\mathbf{F}_7)\cdot\tfrac{1}{2}\delta\mathbf{x}_{74}\wedge\delta\mathbf{x}_{12}+\tfrac{1}{4}(\mathbf{F}_1+\mathbf{F}_6+\mathbf{F}_7+\mathbf{F}_8)\cdot\tfrac{1}{2}\delta x_{67}\wedge\delta\mathbf{x}_{18}$$
$$+\tfrac{1}{4}(\mathbf{F}_2+\mathbf{F}_5+\mathbf{F}_7+\mathbf{F}_8)\cdot\tfrac{1}{2}\delta\mathbf{x}_{57}\wedge\delta\mathbf{x}_{82}+\tfrac{1}{4}(\mathbf{F}_3+\mathbf{F}_5+\mathbf{F}_6+\mathbf{F}_8)\cdot\tfrac{1}{2}\delta\mathbf{x}_{56}\wedge\delta\mathbf{x}_{38}]. \quad (14)$$

This is the discretization adopted in References 6 and 7. The integration rule is exact for linear functions only if the faces are planar parallelograms. Although the method may still be used if this is not the case, only constant functions can be integrated exactly. Thus one might expect the accuracy of this discretization to be severely diminished under mesh distortion. For the special case of the canonical cube $[-1, 1]^3$ this is the unique scheme which will integrate trilinear functions exactly.

It would be a desirable property for the cell residual to be able to integrate linear functions exactly on any mesh, as is the case in one and two dimensions. This may be achieved by triangulating each face and then applying the midpoint rule over the two triangles on each face. Thus each triangle is planar and has a well-defined normal. The midpoint rule will always integrate linear functions exactly on any triangle. Clearly many triangulations are possible, one of which is illustrated in Figure 3. For this triangulation the cell residual is defined as

$$R\approx\frac{1}{V}[\tfrac{1}{3}(\mathbf{F}_3+\mathbf{F}_4+\mathbf{F}_5)\cdot\tfrac{1}{2}\delta\mathbf{x}_{34}\wedge\delta\mathbf{x}_{54}+\tfrac{1}{3}(\mathbf{F}_2+\mathbf{F}_4+\mathbf{F}_5)\cdot\tfrac{1}{2}\delta\mathbf{x}_{54}\wedge\delta\mathbf{x}_{24}$$
$$+\tfrac{1}{3}(\mathbf{F}_1+\mathbf{F}_7+\mathbf{F}_8)\cdot\tfrac{1}{2}\delta\mathbf{x}_{71}\wedge\delta\mathbf{x}_{81}+\tfrac{1}{3}(\mathbf{F}_1+\mathbf{F}_8+\mathbf{F}_6)\cdot\tfrac{1}{2}\delta\mathbf{x}_{81}\wedge\delta\mathbf{x}_{61}$$
$$+\tfrac{1}{3}(\mathbf{F}_4+\mathbf{F}_1+\mathbf{F}_6)\cdot\tfrac{1}{2}\delta\mathbf{x}_{14}\wedge\delta\mathbf{x}_{64}+\tfrac{1}{3}(\mathbf{F}_4+\mathbf{F}_6+\mathbf{F}_3)\cdot\tfrac{1}{2}\delta\mathbf{x}_{64}\wedge\delta\mathbf{x}_{34}$$
$$+\tfrac{1}{3}(\mathbf{F}_8+\mathbf{F}_7+\mathbf{F}_2)\cdot\tfrac{1}{2}\delta\mathbf{x}_{78}\wedge\delta\mathbf{x}_{28}+\tfrac{1}{3}(\mathbf{F}_8+\mathbf{F}_2+\mathbf{F}_5)\cdot\tfrac{1}{2}\delta\mathbf{x}_{28}\wedge\delta\mathbf{x}_{58}$$
$$+\tfrac{1}{3}(\mathbf{F}_4+\mathbf{F}_2+\mathbf{F}_7)\cdot\tfrac{1}{2}\delta\mathbf{x}_{24}\wedge\delta\mathbf{x}_{74}+\tfrac{1}{3}(\mathbf{F}_4+\mathbf{F}_7+\mathbf{F}_1)\cdot\tfrac{1}{2}\delta\mathbf{x}_{74}\wedge\delta\mathbf{x}_{14}$$
$$+\tfrac{1}{3}(\mathbf{F}_8+\mathbf{F}_5+\mathbf{F}_3)\cdot\tfrac{1}{2}\delta\mathbf{x}_{58}\wedge\delta\mathbf{x}_{38}+\tfrac{1}{3}(\mathbf{F}_8+\mathbf{F}_3+\mathbf{F}_6)\cdot\tfrac{1}{2}\delta\mathbf{x}_{38}\wedge\delta\mathbf{x}_{68}]. \quad (15)$$

Clearly there are many different combinations of triangulations. To illustrate this, the stencils of three types of discretizations for linear advection, $\mathbf{F}=(aq, bq, cq)^{\mathrm{T}}$, on a uniform mesh are presented in Figures 4–6. By inspection the triangulated discretizations could be interpreted as upwinding, i.e. choosing the integration rule to maxmize the coefficient of the upwind point. It is

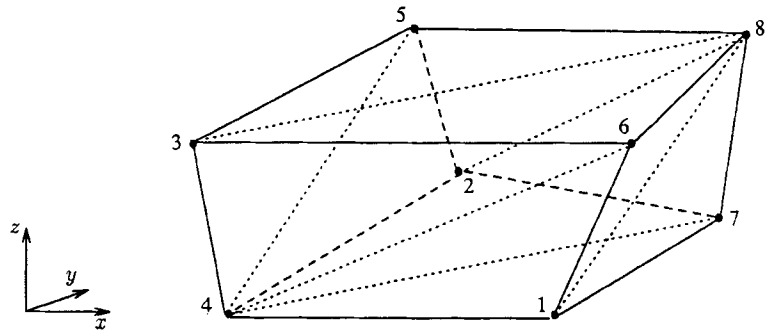

Figure 3. A triangulation of a general eight-point volume

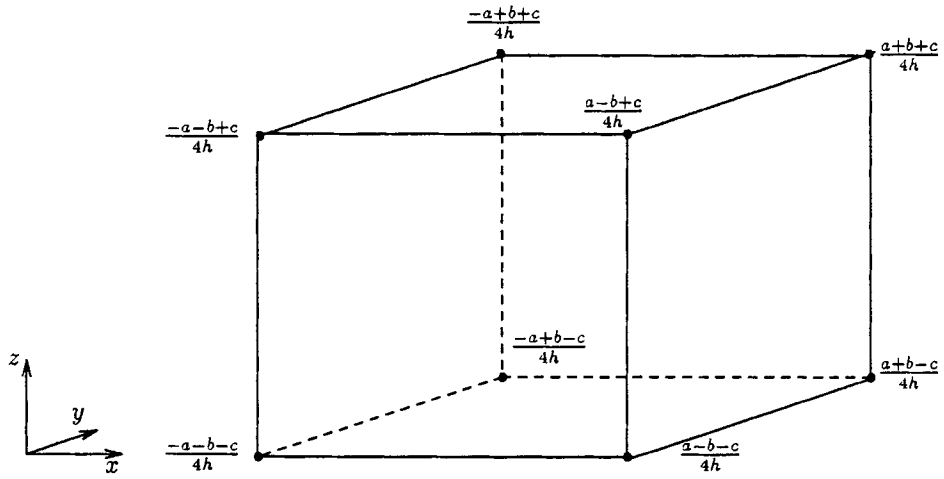

Figure 4. A cell vertex stencil on a uniform mesh where each face is assumed planar

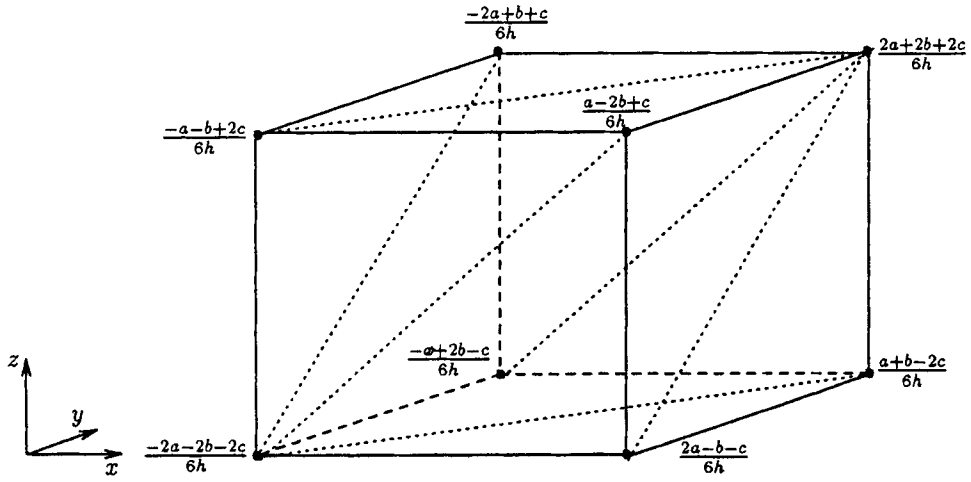

Figure 5. A cell vertex stencil on a uniform mesh with opposite faces triangulated identically

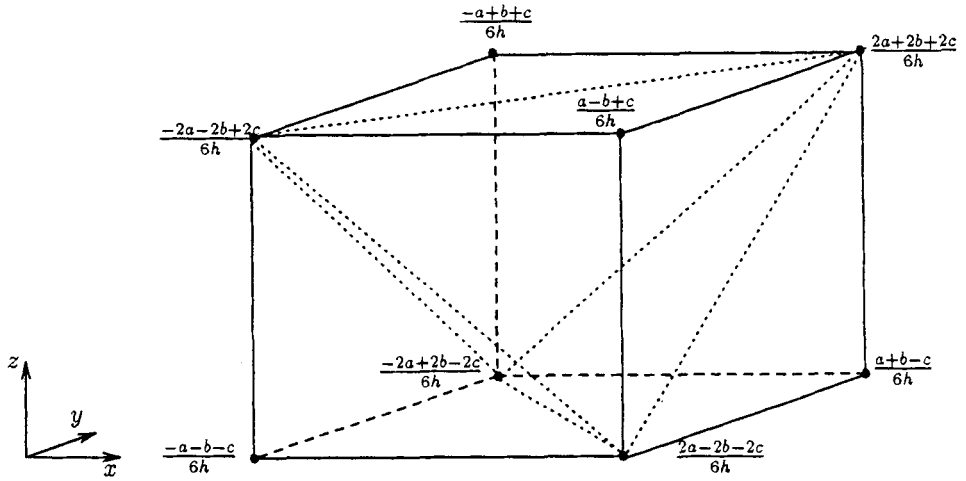

Figure 6. A cell vertex stencil on a uniform mesh with opposite faces triangulated in an opposite manner

worth noting that for conservation throughout any mesh the triangulation of any face needs to be identical for adjacent cell residuals.

It is clear that an eight-point stencil cannot have a second-order truncation error on an irregular mesh, since in general the first 10 terms of the Taylor series need to be set to zero. However, motivated by the cell vertex method in two dimensions, a second-order truncation error is sought on parallelepipeds. The following existence theorem characterizes such methods.

Theorem 2

There exists a one-parameter family of eight-point cell vertex methods for linear advection with second-order truncation error on parallelepipeds. Each member of the family has the following properties:

1. opposite coefficients of the stencil sum to zero;
2. the stencil admits spurious oscillatory solution modes.

Proof. The eight-point discretization may be written

$$\boldsymbol{a}\cdot\nabla q \approx \sum_{i=1}^{8} \alpha_i q_i,$$

where $\boldsymbol{a}=(a, b, c)^{\mathrm{T}}$ is constant and $\{\alpha_i\}_{i=1}^{8}$ are the stencil coefficients ordered as in Figure 2. The centre of the parallelepiped, $\mathbf{x}_0$, is defined as

$$\mathbf{x}_0 = \tfrac{1}{8}\sum_{i=1}^{8} \mathbf{x}_i.$$

Expanding the first 10 terms in the Taylor series about $\mathbf{x}_0$ gives

$$\begin{aligned}\boldsymbol{a}\cdot\nabla q(\mathbf{x}_0) \approx \sum_{i=1}^{8} \alpha_i (&q|_{\mathbf{x}=\mathbf{x}_0} + \delta x_i q_x|_{\mathbf{x}=\mathbf{x}_0} + \delta y_i q_y|_{\mathbf{x}=\mathbf{x}_0} + \delta z_i q_z|_{\mathbf{x}=\mathbf{x}_0} \\ &+ \delta x_i \delta y_i q_{xy}|_{\mathbf{x}=\mathbf{x}_0} + \delta x_i \delta z_i q_{xz}|_{\mathbf{x}=\mathbf{x}_0} + \delta y_i \delta z_i q_{yz}|_{\mathbf{x}=\mathbf{x}_0} \\ &+ \frac{\delta x_i^2}{2} q_{xx}|_{\mathbf{x}=\mathbf{x}_0} + \frac{\delta y_i^2}{2} q_{yy}|_{\mathbf{x}=\mathbf{x}_0} + \frac{\delta z_i^2}{2} q_{zz}|_{\mathbf{x}=\mathbf{x}_0}),\end{aligned} \tag{16}$$

where $\delta\mathbf{x}_i=(\delta x_i, \delta y_i, \delta z_i)^T=\mathbf{x}_i-\mathbf{x}_0$. Let

$$\mathbf{l}=(1,1,1,1)^T, \qquad \mathbf{A}=\begin{pmatrix} \delta x_1 & \delta x_2 & \delta x_3 & \delta x_4 \\ \delta y_1 & \delta y_2 & \delta y_3 & \delta y_4 \\ \delta z_1 & \delta z_2 & \delta z_3 & \delta z_4 \end{pmatrix},$$

$$\mathbf{B}=\begin{pmatrix} \delta x_1\delta y_1 & \delta x_2\delta y_2 & \delta x_3\delta y_3 & \delta x_4\delta y_4 \\ \delta x_1\delta z_1 & \delta x_2\delta z_2 & \delta x_3\delta z_3 & \delta x_4\delta z_4 \\ \delta y_1\delta z_1 & \delta y_2\delta z_2 & \delta y_3\delta z_3 & \delta y_4\delta z_4 \end{pmatrix}, \qquad \mathbf{C}=\begin{pmatrix} (\delta x_1)^2 & (\delta x_2)^2 & (\delta x_3)^2 & (\delta x_4)^2 \\ (\delta y_1)^2 & (\delta y_2)^2 & (\delta y_3)^2 & (\delta y_4)^2 \\ (\delta z_1)^2 & (\delta z_2)^2 & (\delta z_3)^2 & (\delta z_4)^2 \end{pmatrix}.$$

On a parallelepiped

$$\delta\mathbf{x}_i=-\delta\mathbf{x}_{i+4}, \qquad i=1,\ldots,4.$$

Equating derivatives in equation (16) gives a second-order truncation error provided that

$$\begin{pmatrix} \mathbf{l}^T & \mathbf{l}^T \\ A & -A \\ B & B \\ C & C \end{pmatrix}\begin{pmatrix} \alpha_1 \\ \vdots \\ \alpha_8 \end{pmatrix}=\begin{pmatrix} 0 \\ \boldsymbol{a} \\ \mathbf{0} \\ \mathbf{0} \end{pmatrix},$$

where $\mathbf{0}=(0,0,0)^T$. Changing variables to

$$\beta_i=\alpha_i+\alpha_{i+4} \quad \text{and} \quad \gamma_i=\alpha_i-\alpha_{i+4}, \qquad i=1,\ldots,4, \tag{17}$$

results in

$$\begin{pmatrix} \mathbf{0}^T & \mathbf{l}^T \\ A & 0 \\ 0 & B \\ 0 & C \end{pmatrix}\begin{pmatrix} \boldsymbol{\gamma} \\ \boldsymbol{\beta} \end{pmatrix}=\begin{pmatrix} 0 \\ \boldsymbol{a} \\ \mathbf{0} \\ \mathbf{0} \end{pmatrix},$$

where $\boldsymbol{\gamma}=(\gamma_1,\ldots,\gamma_4)^T$ and $\boldsymbol{\beta}=(\beta_1,\ldots,\beta_4)^T$. This decouples to

$$\mathbf{A}\boldsymbol{\gamma}=\boldsymbol{a} \tag{18}$$

and

$$\begin{pmatrix} \mathbf{l}^T \\ B \\ C \end{pmatrix}\boldsymbol{\beta}=\begin{pmatrix} 0 \\ \vdots \\ 0 \end{pmatrix}. \tag{19}$$

If the matrix $(\mathbf{l}^T, B, C)^T$ is of rank four than $\boldsymbol{\beta}=\mathbf{0}$ and property 1 follows immediately. In order to show this, it is advantageous to parametrize the parallelepiped, without any loss of generality, as in Figure 7. The constants r, s and t represent shear factors in the xz-, yz- and xy-planes respectively. With this parametrization the centre of the parallelepiped is given by

$$\mathbf{x}_0=(x_0, y_0, z_0)^T=(h_x+r+t, h_y+s, h_z)^T$$

and hence the relevant distances are

$$\begin{aligned} &\delta x_1=h_x-r-t, && \delta x_2=-h_x-r+t, && \delta x_3=-h_x+r-t, && \delta x_3=h_x-r-t, \\ &\delta y_1=-h_y-s, && \delta y_2=h_y-s, && \delta y_3=-h_y+s, && \delta y_3=-h_y-s, \\ &\delta z_1=-h_z, && \delta z_2=-h_z, && \delta z_3=h_z, && \delta z_3=-h_z. \end{aligned}$$

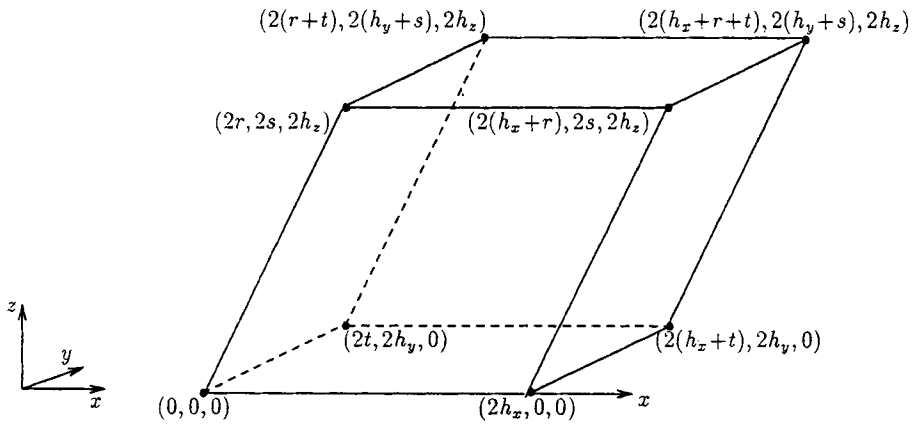

Figure 7. The parametrization of a general parallelepiped

Thus the first four rows of the matrix $(\mathbf{I}^{\mathrm{T}}, B, C)^{\mathrm{T}}$ may be written

$$\begin{pmatrix} 1 & 1 & 1 & 1 \\ (r+t-h_x)(h_y+s) & (t-h_x-r)(h_y-s) & (r-h_x-t)(s-h_y) & (h_x+r+t)(h_y+s) \\ (r+t-h_x)h_z & (h_x+r-t)h_z & (r-h_x-t)h_z & (h_x+r+t)h_z \\ (h_y+s)h_z & (s-h_y)h_z & (s-h_y)h_z & (h_y+s)h_z \end{pmatrix}$$

whose determinant is

$$-16h_x^2h_y^2h_z^2 = -V^2/4,$$

where V is the volume of the parallelepiped. Hence $\boldsymbol{\beta}=\mathbf{0}$ for all non-trivial volumes and property 1 follows.

To show the existence of a one-parameter family, note that on a parallelepiped

$$\delta\mathbf{x}_4 = \sum_{i=1}^{3} \delta\mathbf{x}_i \tag{20}$$

and define the triple scale product

$$[\delta\mathbf{x}_1, \delta\mathbf{x}_2, \delta\mathbf{x}_3] = \delta\mathbf{x}_1 \cdot (\delta\mathbf{x}_2 \wedge \delta\mathbf{x}_3) = V/2. \tag{21}$$

Given that $\boldsymbol{\beta}=\mathbf{0}$, then from (17) $\gamma_i = 2\alpha_i$ for $i=1, \ldots, 4$. Thus equation (18) may be written

$$2(\alpha_1\delta\mathbf{x}_1 + \alpha_2\delta\mathbf{x}_2 + \alpha_3\delta\mathbf{x}_3 + \alpha_4\delta\mathbf{x}_4) = \boldsymbol{a}. \tag{22}$$

Thus, using equation (20), this becomes

$$2[(\alpha_1+\alpha_4)\delta\mathbf{x}_1 + (\alpha_2+\alpha_4)\delta\mathbf{x}_2 + (\alpha_3+\alpha_4)\delta\mathbf{x}_3] = \boldsymbol{a}. \tag{23}$$

This is a 3×3 matrix system whose determinant is $[\delta\mathbf{x}_1, \delta\mathbf{x}_2, \delta\mathbf{x}_3]$; hence from (21) it is non-singular. Cramer's rule gives

$$\alpha_1 + \alpha_4 = -(1/V)[\boldsymbol{a}, \delta\mathbf{x}_2, \delta\mathbf{x}_3], \tag{24}$$

$$\alpha_2 + \alpha_4 = (1/V)[\boldsymbol{a}, \delta\mathbf{x}_1, \delta\mathbf{x}_3], \tag{25}$$

$$\alpha_3 + \alpha_4 = -(1/V)[\boldsymbol{a}, \delta\mathbf{x}_1, \delta\mathbf{x}_2]. \tag{26}$$

Introducing a single parameter ϕ, a family of cell vertex discretizations with second-order truncation error on parallelepipeds can be described by defining

$$\alpha_4=(1/4V)([\boldsymbol{a},\delta\mathbf{x}_1,\delta\mathbf{x}_3]-[\boldsymbol{a},\delta\mathbf{x}_1,\delta\mathbf{x}_2]-[\boldsymbol{a},\delta\mathbf{x}_2,\delta\mathbf{x}_3])+\phi=-\alpha_8.$$

Using (24)–(26) and (22),

$$\alpha_1=(1/4V)([\boldsymbol{a},\delta\mathbf{x}_3,\delta\mathbf{x}_4]-[\boldsymbol{a},\delta\mathbf{x}_2,\delta\mathbf{x}_4]-[\boldsymbol{a},\delta\mathbf{x}_2,\delta\mathbf{x}_3])-\phi=-\alpha_5,$$

$$\alpha_2=(1/4V)([\boldsymbol{a},\delta\mathbf{x}_1,\delta\mathbf{x}_3]+[\boldsymbol{a},\delta\mathbf{x}_1,\delta\mathbf{x}_4]-[\boldsymbol{a},\delta\mathbf{x}_3,\delta\mathbf{x}_4])-\phi=-\alpha_6,$$

$$\alpha_3=(1/4V)([\boldsymbol{a},\delta\mathbf{x}_2,\delta\mathbf{x}_4]-[\boldsymbol{a},\delta\mathbf{x}_2,\delta\mathbf{x}_2]-[\boldsymbol{a},\delta\mathbf{x}_1,\delta\mathbf{x}_4])-\phi=-\alpha_7,$$

for sufficiently small ϕ to be discussed later.

It remains to show that all these stencils admit high-frequency oscillatory modes. This is proved by seeking solutions of the homogeneous equations of the form

$$q_{ijk}=\Theta_1^i\Theta_2^j\Theta_3^k,$$

where q_{ijk} defines some regular parallelepiped (i, j, k) mesh. Substituting this into the stencil gives

$$\alpha_4(1-\Theta_1\Theta_2\Theta_3)+\alpha_1(\Theta_1-\Theta_2\Theta_3)+\alpha_2(\Theta_2-\Theta_1\Theta_3)+\alpha_3(\Theta_3-\Theta_1\Theta_2)=0. \tag{27}$$

All the terms in parentheses clearly go to zero for the consistency condition $\Theta=(1, 1, 1)^{\mathrm{T}}$. However, they also vanish when

$$\Theta=(1,-1,-1)^{\mathrm{T}},(-1,1,-1)^{\mathrm{T}},(-1,-1,1)^{\mathrm{T}}, \tag{28}$$

which represent high-frequency oscillatory modes undetected by the stencil. In addition, if $\Theta=(-1,-1,-1)^{\mathrm{T}}$ then (27) becomes

$$2(\alpha_4-\alpha_1-\alpha_2-\alpha_3)=4\phi; \tag{29}$$

hence if $\phi=0$, an extra oscillatory mode is introduced. Thus the proof of the theorem is complete. □

The following general remarks are consequences of the theorem.

1. The case $\phi=0$ is equivalent to equation (14) on a parallelepiped. Furthermore, the triangulated discretization given in equation (15) is obtained for

$$\phi=(1/2V)(-[\boldsymbol{a},\delta\mathbf{x}_1,\delta\mathbf{x}_2]+[\boldsymbol{a},\delta\mathbf{x}_1,\delta\mathbf{x}_3]-[\boldsymbol{a},\delta\mathbf{x}_2,\delta\mathbf{x}_3]). \tag{30}$$

   Hence these methods derived through the finite volume formulation have second-order truncation error. However, the triangulation given in Figure 6 is only of first order since $\boldsymbol{\beta}\neq\mathbf{0}$. In fact, for constant coefficient linear advection second-order accuracy can only be obtained if opposite faces are triangulated identically.
2. A non-zero ϕ is effectively adding a chequerboard into the stencil which on a uniform mesh approximates the mixed derivative term $\phi h^3 q_{xyz}$. To retain second-order accuracy, ϕ must be $O(h^{-1})$, which is the same order as the other terms in equation (14). The ϕ given in equation (30) satisfies this constraint. The choice of non-zero ϕ has a beneficial effect on the spectral properties of the discretization since fewer oscillatory modes are admitted. In two dimensions adding a chequerboard into the stencil has been studied in Reference 8 and is equivalent to a term $\phi h^2 q_{xy}$. To retain a second-order truncation error, ϕ has to be $O(1)$, which is of lower order than the other terms in equation (13). Thus the beneficial effects of this additional term are diminished as the mesh is refined.

3. The three-dimensional existence theorem, the two-dimensional uniqueness theorem and the above note all illustrate the greater flexibility available to the cell vertex method in three dimensions. The existence of a one-parameter family of second-order methods in three dimensions suggests the possibility of optimizing the spectral properties in order to improve the convergence of iterative methods.

3.1. Fourier Analysis

In order to examine the spectral properties of these stencils in more detail, a straightforward Fourier analysis is presented for a uniform mesh. A Fourier symbol $S(\boldsymbol{\theta})$ is sought such that

$$\sum_{i=1}^{8} \alpha_i q(\mathbf{x}_i) = S(\boldsymbol{\theta}) q(\mathbf{x}_0), \tag{31}$$

with q defined by

$$q(\mathbf{x}) = \exp\left(\frac{i}{h}(\boldsymbol{\theta} \cdot \mathbf{x})\right) \tag{32}$$

and $\boldsymbol{\theta} = (\theta_1, \theta_2, \theta_3)^T \in (-\pi, \pi]^3$. Substituting (32) in (31) and using $\boldsymbol{\beta} = \mathbf{0}$,

$$S(\boldsymbol{\theta}) = 2i\alpha_1 \sin\left(\frac{\theta_1 - \theta_2 - \theta_3}{2}\right) + 2i\alpha_2 \sin\left(\frac{-\theta_1 + \theta_2 - \theta_3}{2}\right) + 2i\alpha_3 \sin\left(\frac{-\theta_1 - \theta_2 + \theta_3}{2}\right)$$
$$+ 2i\alpha_4 \sin\left(\frac{-\theta_1 - \theta_2 - \theta_3}{2}\right). \tag{33}$$

The zeros of $S(\boldsymbol{\theta})$ represent modes which the discretization cannot detect. The corresponding functions $q(\mathbf{x})$ model eigenfunctions of the discretization with small eigenvalues. They are thus a crucial indication of the likely performance of iterative solvers. Firstly, the high-frequency modes on the sides of the Fourier cube are examined. For $\theta_1 = \pi$ equation (33) becomes

$$S(\boldsymbol{\theta}) = i\left[\left(\frac{a}{h} - 4\phi\right)\cos\left(\frac{\theta_2 + \theta_3}{2}\right) + \left(\frac{a}{h} + 4\phi\right)\cos\left(\frac{\theta_2 - \theta_3}{2}\right)\right]. \tag{34}$$

If $\theta_2 = \pi$ then

$$S(\boldsymbol{\theta}) = 8i\phi \sin\left(\frac{\theta_3}{2}\right). \tag{35}$$

Hence $S(\boldsymbol{\theta}) = 0$ for $\boldsymbol{\theta} = (\pi, \pi, 0)^T$. Similarly, there are additional zeros along every edge of the Fourier cube at the points

$$\boldsymbol{\theta} = (\pi, \pi, 0)^T, (\pi, 0, \pi)^T, (0, \pi, \pi)^T. \tag{36}$$

These are the modes represented in equation (28). For $\phi = 0$ the symbol also vanishes along the edge $\boldsymbol{\theta} = (\pi, \pi, \psi)^T$ for all $\psi \in (-\pi, \pi]$ and in general for

$$\boldsymbol{\theta} = (\pi, \pi, \psi)^T, (\pi, \psi, \pi)^T, (\psi, \pi, \pi)^T \tag{37}$$

for all $\psi \in (-\pi, \pi]$. These modes correspond to those of equation (29). It is easy to show from (34) that $S(\boldsymbol{\theta})$ is non-zero at the modes

$$\boldsymbol{\theta} = (\pm\pi, 0, 0)^T, (0, \pm\pi, 0)^T, (0, 0, \pm\pi)^T \tag{38}$$

if all components of $\boldsymbol{\alpha}$ are non-zero.

Finally, consider the symbol in the neighbourhood of the origin. The consistency condition $S(\mathbf{0})=0$ holds. Furthermore, for small θ the approximation $\sin(\theta_i)\approx\theta_i$ leads to

$$S(\theta)\approx\frac{\mathrm{i}}{16h}\,\alpha\cdot\theta.$$

Hence the symbol vanishes for small θ orthogonal to α. This result represents a physical characteristic mode illustrating that low-frequency error is not propagated orthogonally to streamlines. A similar result is true in two dimensions.[5] Away from the origin these characteristic zeroes of S deviate to coalesce with the modes (36)–(38) as illustrated by the following figures.

Three-dimensional representations of the Fourier symbol $S(\theta)$ for the discretisations in Figures 4 and 5 are illustrated in Figure 8. These are grey-shaded contour plots of S projected onto slices

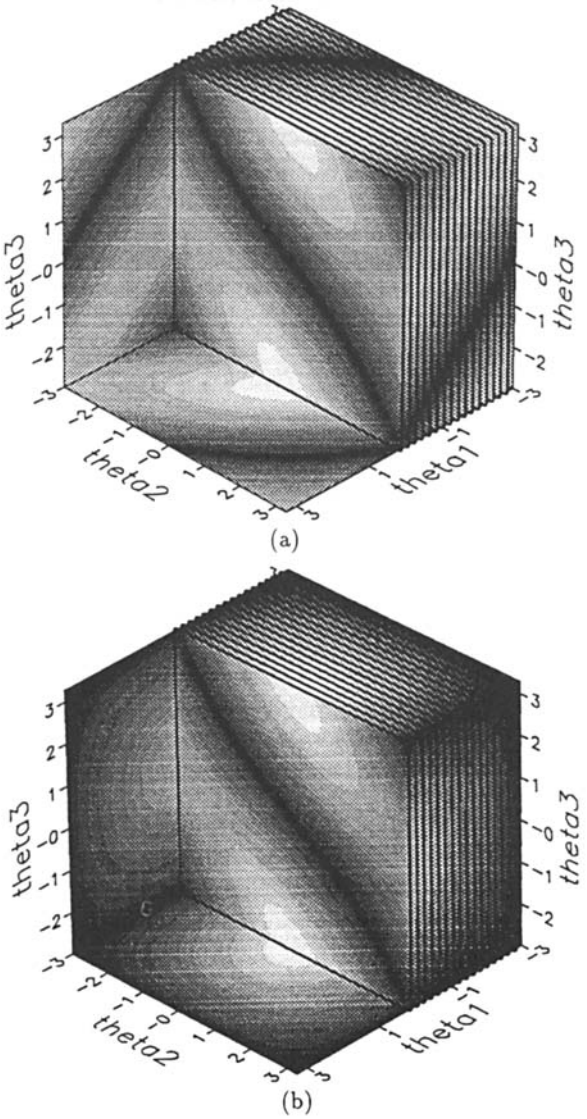

Figure 8. A three-dimensional representation of the Fourier symbol $S(\theta)$—the dark areas represent a small symbol: (a) triangulated faces, as in Figure 5; (b) non-triangulated faces, as in Figure 4; $\alpha=(1, 2, 3)^{\mathrm{T}}$

of the cube $[-\pi, \pi]^3$. The dark regions show where the symbol vanishes. The point zeros on the exterior, given by equation (36), and the characteristic central zeros, given in equation (38), of the Fourier cube are clearly illustrated for both discretizations. The symbol of the triangulated discretization, Figure 8(a), only vanishes over a single surface connecting the central and exterior zeros. It is immediately apparent that the nontriangulated symbol, Figure 8(b), also vanishes over all edges of the Fourier cube represented by equation (37). This means that the non-triangulated scheme has an extra dimension of high-frequency Fourier modes which are undetected by the stencil. The convergence of iterative solvers is well known to be severely inhibited by the existence of high-frequency zeros within the Fourier symbol.[5]

4. NUMERICAL RESULTS

4.1. Constant flow field

This section investigates the achieved global order of accuracy of the two cell vertex discretizations discussed above. These will be referred to as the planar method (see Figure 2 and equation (14)) and the triangulated method (see Figure 3 and equation (15)). These discretizations are tested on stretched, skewed, randomly distorted meshes. The first test problem is, as for the theorem, linear advection with constant coefficients,

$$\boldsymbol{a} \cdot \nabla q = 0,$$

where $\boldsymbol{a} = (a, b, c)^{\mathrm{T}}$ is fixed. The general solution is

$$q = Q(u, v),$$

where

$$u = cx - az, \qquad v = cy - bz$$

for some arbitrary differentiable function Q. For the purpose of this study the function

$$Q(u, v) = \sin(\pi u) \sin(\pi v) \tag{39}$$

was chosen with $\boldsymbol{a} = (\frac{1}{3}, \frac{2}{3}, 1)^{\mathrm{T}}$. This smooth function was chosen in order that asymptotic rates of convergence could be achieved on relatively coarse meshes.

Grids were generated by distorting a uniform mesh on a unit cube given by

$$x_{i,j,k} = (i-1)h, \quad y_{i,j,k} = (j-1)h \quad \text{and} \quad z_{i,j,k} = (k-1)h, \qquad i, j, k = 1, \ldots, N,$$

where $h = 1/(N-1)$ for some mesh size N. In order to demonstrate where the second-order accuracy of the methods breaks down, each interior point was randomly perturbed within a ball of radius $h/2$:

$$x_{i,j,k} := x_{i,j,k} + \chi \frac{\eta}{200} h, \qquad i = 2, \ldots, N-1, \quad j, k = 1, \ldots, N,$$

$$y_{i,j,k} := y_{i,j,k} + \chi \frac{\eta}{200} h, \qquad j = 2, \ldots, N-1, \quad i, k = 1, \ldots, N,$$

$$z_{i,j,k} := z_{i,j,k} + \chi \frac{\eta}{200} h, \qquad k = 2, \ldots, N-1, \quad i, j = 1, \ldots, N,$$

for some $\chi \in [0, 100]$ and random number $\eta \in [-1, 1]$. The parameter η represents a percentage of random perturbation. For $\eta > 100$ mesh overlap would be possible. To model the types of meshes

essential for advection–diffusion and Navier–Stokes computations, the mesh was stretched using the function

$$w(\xi, \mu) = \begin{cases} \operatorname{sgn}(\xi) \dfrac{\exp(-\mu|\xi|)-1}{\exp(-\mu)-1}, & \mu \neq 0, \\ 0, & \mu = 0, \end{cases}$$

by

$$x_{i,j,k} := w(x_{i,j,k}, \mu), \quad y_{i,j,k} := w(y_{i,j,k}, \mu) \quad \text{and} \quad z_{i,j,k} := w(z_{i,j,k}, \mu), \qquad i, j, k = 1, \ldots, N,$$

for some given μ. Hence for $\mu > 0$ all the point are stretched towards the faces $x = 1$, $y = 1$ and $z = 1$ of the unit cube. Finally, to test the results of the theorem regarding skewed control volumes, the stretched randomized mesh was mapped onto a general parallelepiped in a similar fashion to Figure 7 by

$$x_{i,j,k} := x_{i,j,k} + 2rz_{i,j,k} + 2ty_{i,j,k}, \quad y_{i,j,k} := y_{i,j,k} + 2sz_{i,j,k} \quad \text{and} \quad z_{i,j,k} := z_{i,j,k}, \quad i, j, k = 1, \ldots, N,$$

for some r, s and t. Hence, by using the parameters μ, η and r, s, t, a uniform mesh on a cube can be severely distorted. An example of such a mesh is given in Figure 9.

Throughout these results $\boldsymbol{a}$ was fixed at $(\frac{1}{3}, \frac{2}{3}, 1)^T$. To ensure that the numerical domain of dependence lay within the analytical domain of dependence, (r, s, t) was chosen to be $(-\frac{1}{8}, -\frac{1}{4}, \frac{1}{4})$. Using the analytical solution given by equation (39), Dirichlet boundary data were specified on the mesh planes $i = 1, j = 1$ and $k = 1$. Hence the test problem is to advect the sine function along the vector $(\frac{1}{3}, \frac{2}{3}, 1)^T$.

The cell vertex method leads to a system of cell-based equations in terms of node-based unknowns. For this test problem there are N^3 unknowns $q_{i,j,k}$, $i, j, k = 1, \ldots, N$. There are

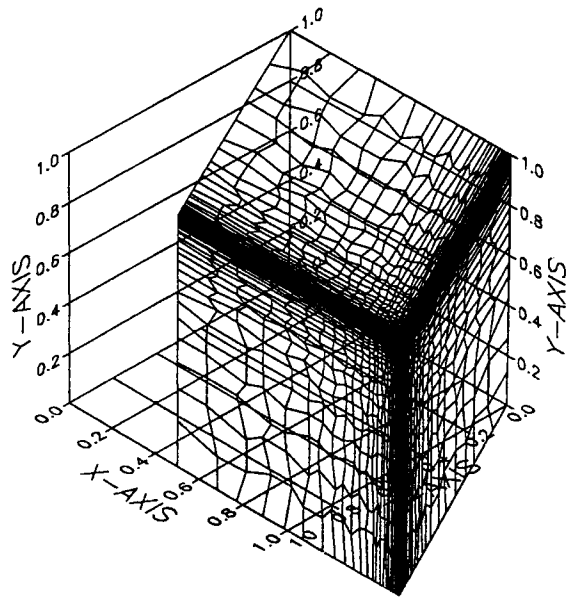

Figure 9. An example of randomly perturbed, stretched, skewed $(20 \times 20 \times 20)$ mesh with $r = 20\%$, $\mu = 5$ and $(r, s, t) = (\frac{1}{4}, 0, 0)$

$(N-1)^3$ cell-based residual equations and three planes of Dirichlet data, giving $3(N-1)^2+3(N-1)+1=N^3$ equations in N^3 unknowns. Thus the counting is correct. As will be seen later, it is not always obvious that the numbers of unknowns and equations are equal. For more details of the counting difficulties associated with cell vertex systems and how they may be overcome see References 9 and 10.

Ordering the unknowns $q_{i,j,k} \approx q(\mathbf{x}_{i,j,k})$ lexicographically, a lower triangular matrix may be obtained. For this linear test problem this matrix may be simply inverted by one Gauss–Seidel iteration, which is equivalent to forward substitution.

To illustrate the order of accuracy achieved, the global error is assumed to be of the form

$$\| \text{error} \| = c\left(\frac{1}{N-1}\right)^p + \text{higher-order terms}$$

for some constant c and order of accuracy p. Ignoring higher-order terms,

$$\log(\| \text{error} \|) = p \log\left(\frac{1}{N-1}\right) + \log c.$$

Hence with the analytical solution (39) available, by plotting $\log(\| \text{error} \|)$ against $\log[1/N-1)]$, the achieved asymptotic order of accuracy of a method is given by the gradient of the curve. The root mean square norm was used to measure the error.

Figure 10 compares the planar and triangulated discretizations for successively stretched meshes, with the lowest curve representing $\mu=0$, the next highest $\mu=2{\cdot}5$, then $\mu=5$. As an indication of the severity of the stretching in the case $\mu=5$ the maximum ratio of volumes on a given mesh is 10^6. It is clear that all the curves demonstrate global second-order accuracy in accordance with the theory. It is worth noting that for the non-stretched case $\mu=0$ a greater total accuracy is achieved by the planar method than by the triangulated method. This advantage is lost as the mesh is stretched. For the case $\mu=5$ the two methods give identical curves.

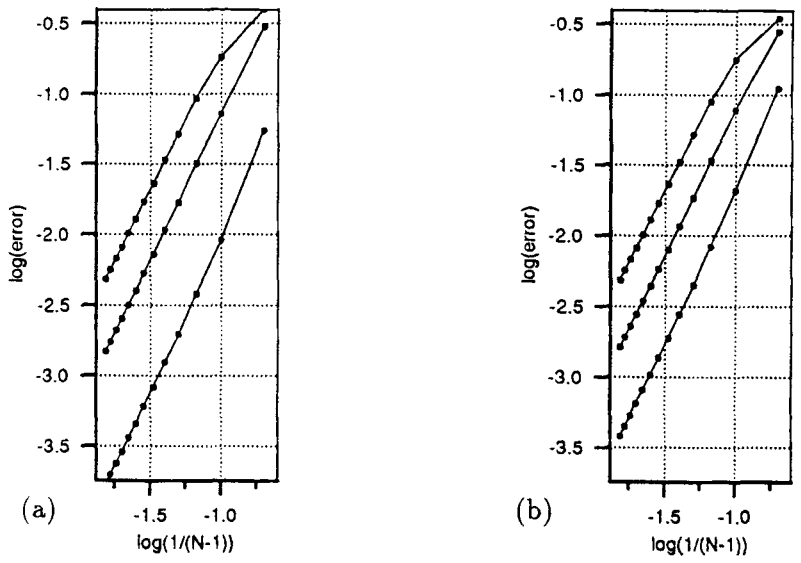

Figure 10. Convergence of (a) planar and (b) triangulated methods on successively stretched parallelepiped meshes; $(r, s, t)=(-\frac{1}{8}, -\frac{1}{4}, \frac{1}{4})$, $\mu=0, 2{\cdot}5, 5$

Figure 11 compares the two discretizations for successively randomized meshes. The lowest curve represents the case $\eta = 0\%$, with the higher curves illustrating increments of η by 10% until no convergence can be observed. The triangulated method maintains second-order accuracy up to $\eta = 30\%$ whereas the planar method breaks down at $\eta = 10\%$. The triangulated method is thus clearly superior on random meshes. The original motivation for triangulating the control

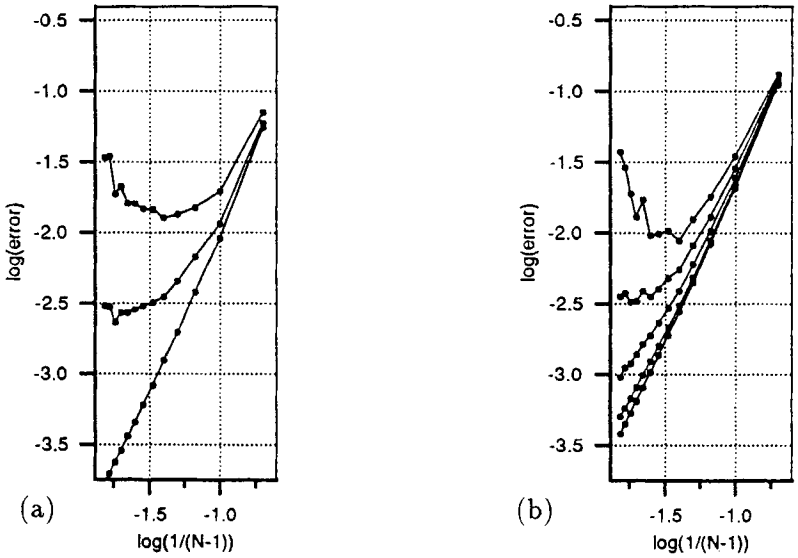

Figure 11. Convergence of (a) planar and (b) triangulated methods on successively randomized meshes; $(r, s, t) = (-\frac{1}{8}, -\frac{1}{4}, \frac{1}{4})$, $\mu = 0$, with η increasing from zero in increments of 10

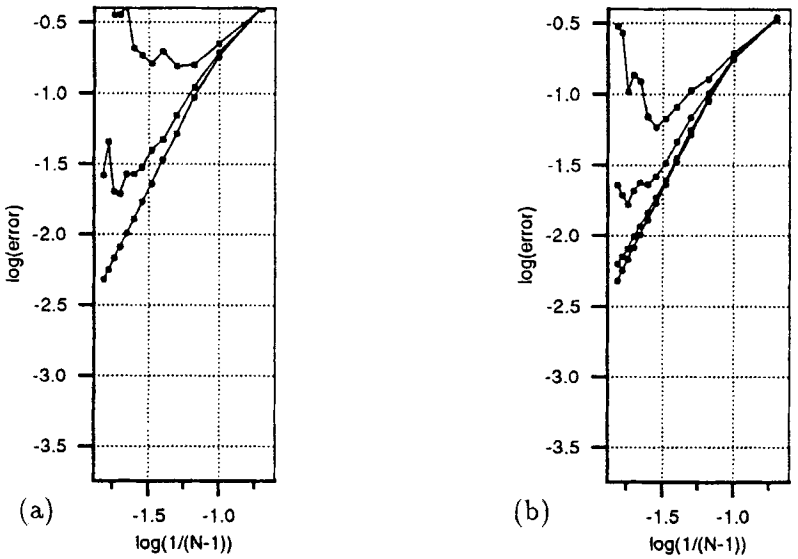

Figure 12. Convergence of (a) planar and (b) triangulated methods on successively randomized stretched meshes; $(r, s, t) = (-\frac{1}{8}, -\frac{1}{4}, \frac{1}{4})$, $\mu = 5$, with η increasing from zero in increments of 10

volumes was to enhance the integration rule over non-planar faces, as is the case with these random meshes. It is therefore not surprising that the triangulated discretization is significantly more accurate than the planar method. Figure 12 reinforces this point by performing the same experiment as Figure 11 but with a stretching parameter $\mu = 5$. Even for a mesh similar to Figure 9 the triangulated method shows signs of convergence where the planar method does not.

The method of Figure 6 was also tested on uniform meshes. This method is not a member of the one-parameter family and therefore has a first-order truncation error. Numerical experiments exhibited first-order global accuracy. No supraconvergence was observed, as is sometimes the case with conservative finite volume schemes.

The theory suggests that there are many other triangulated discretizations which have a second-order truncation error. The one given in Figure 3 was chosen because for the case where the components of $\boldsymbol{a}$ have the same sign, as in these experiments, this is the triangulation which maximizes the coefficient of the most upwind point. Hence the most favourable method was chosen, giving the most diagonally dominant and thus stable matrix. However, the accuracy of this method is dependent on the flow direction, which is not the case for the planar method. The least favourable method exhibits second-order convergence only on uniform meshes. This is thought to be due to loss of stability. A triangulation independent of the flow direction may be obtained by triangulating each face twice and averaging. On meshes with planar faces this is equivalent to the planar method, but the schemes are distinct on random meshes. Figure 13 illustrates that this method gives little significant improvement over the planar method on random meshes.

4.2. Variable flow fields

In the case of a constant flow field $\boldsymbol{a}$, Theorem 2 states that a second-order truncation error can only be obtained on parallelepipeds if opposite coefficients of the stencil sum to zero. In terms of

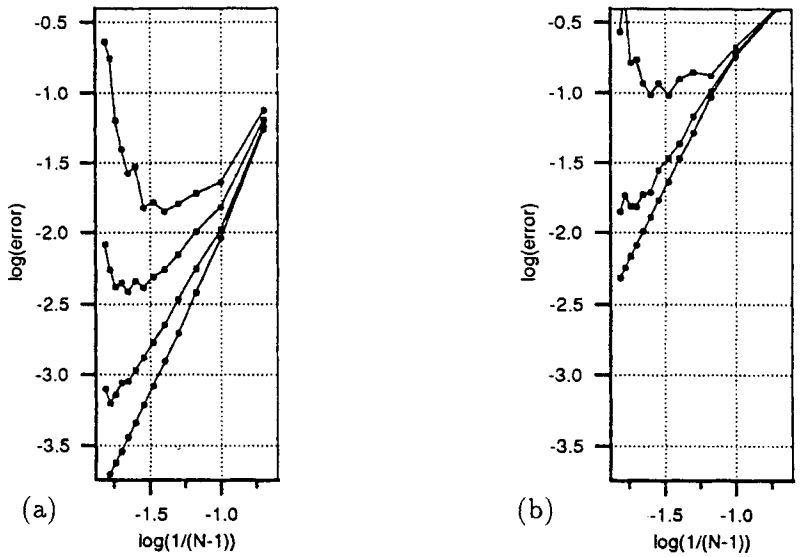

Figure 13. Convergence of averaged triangulation method: (a) successively randomized meshes, $\mu = 0$; (b) successively randomized stretched meshes, $\mu = 5$; $(r, s, t) = (-\frac{1}{8}, -\frac{1}{4}, \frac{1}{4})$, with η increasing from zero in increments of 10

triangulation schemes this means that opposite faces of a hexahedral control volume must be triangulated in the same manner. Conservation further requires that a given face is triangulated in the same direction in adjacent control volumes. Taken together, these constraints imply that all control volumes are triangulated identically throughout the mesh. This represents a major restriction on the choice of method.

For a general flow field these constraints could lead to a non-optimal triangulation in particular regions of the domain. As observed in Section 4.1, a method which is not triangulated in order to maximize diagonal dominance will not achieve second-order convergence on non-uniform meshes. For variable $\boldsymbol{a}$ it is important that a method satisfies the conservation constraint. However, it is not necessarily true that opposite coefficients should sum to zero, since Theorem 2 does not apply to variable $\boldsymbol{a}$.

This is illustrated by the following variable coefficient linear advection problem:

$$\hat{a}q_x + \hat{b}q_y + \hat{c}q_z = 0,$$
$$\hat{\boldsymbol{a}} = (\hat{a}, \hat{b}, \hat{c})^{\mathrm{T}} = [a - \omega(cy - bz),\ b + \omega(cx - az),\ c]^{\mathrm{T}},$$

with true solution

$$q(x, y, z) = Q\left[(cx - az)^2 + (cy - bz)^2,\ \omega z - \tan^{-1}\left(\frac{cy - bz}{cx - az}\right)\right] \tag{40}$$

for some arbitrary differentiable function Q. The problem is solved within a parallelepiped derived by shearing the cube $(x, y, z) \in [-1, 1]^2 \times [0, 2]$ along the vector $\boldsymbol{a} = (a, b, c)^{\mathrm{T}}$ as shown in Figure 14. Each characteristic is a sheared helix of fixed radius and axis $\boldsymbol{a}$. The axis itself is also a characteristic. A solution prescribed on the plane $z = 0$ rotates about $\boldsymbol{a}$ with angular velocity ω as z increases. The solution on the upper plane $z = 2$ is therefore a rotation of the solution prescribed $z = 0$. A qualitative measure of accuracy may therefore be obtained by plotting the approximate solution on these two planes (see Figure 19). A quantitative measure of accuracy is obtained by calculating the error norm using (40).

The triangulation adopted here maximizes the coefficient of the upwind node in each cell by evaluating $\boldsymbol{a}$ at the centre of the cell and triangulating all the upwind faces as for the optimal triangulation in the constant coefficient case. For the given test problem this recipe triangulates all interior faces without ambiguity and is thus conservative. Remaining boundary faces are triangulated in the same fashion as the opposite faces within the cell. The method is therefore conservative, but opposite stencil coefficients do not in general sum to zero.

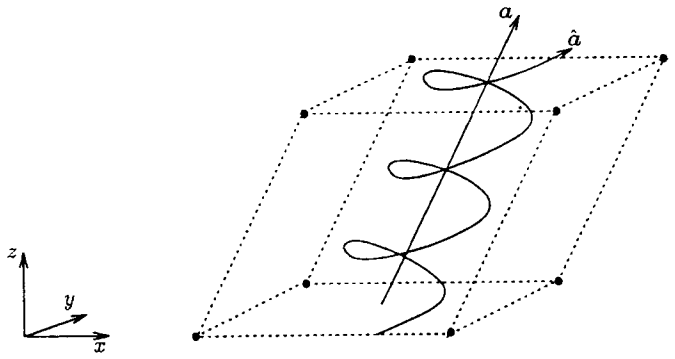

Figure 14. Helical test problem

Randomly perturbed, stretched, sheared meshes were generated as in Section 4.1, with the exception that a node was maintained at the centre of all xy-planes to model the characteristic $\boldsymbol{a}$. Dirichlet boundary conditions were imposed on the plane $z=0$ and on each xy-plane at nodes where the velocity field was strictly incoming. Figure 15 illustrates a typical xy-plane for a uniform mesh. The arrows represent the flow direction and boundary conditions are imposed at nodes denoted by dark squares. On an $N \times N \times N$ mesh there are N^3 unknowns, $(N-1)^3$ cell residuals, N^2 boundary conditions on $z=0$ and $2(N-1)^2$ inflow boundary conditions on the sides of the parallelepiped. Hence there are $N-1$ fewer equations than unknowns. This counting difficulty is rectified by recognizing that the solution at the central node of each xy-plane is not an unknown but is constant along the characteristic $\boldsymbol{a}$. Thus $N-1$ extra *characteristic boundary conditions* are imposed at the nodes denoted by triangles in Figure 15. The resulting system of cell

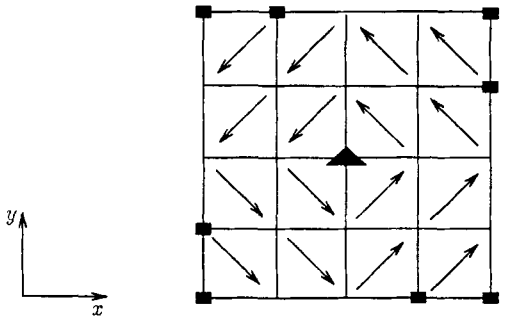

Figure 15. The associations of residuals to unknowns within an xy-plane of the helical test problem. Dark squares denote inlet boundary conditions. The triangle denotes a characteristic condition

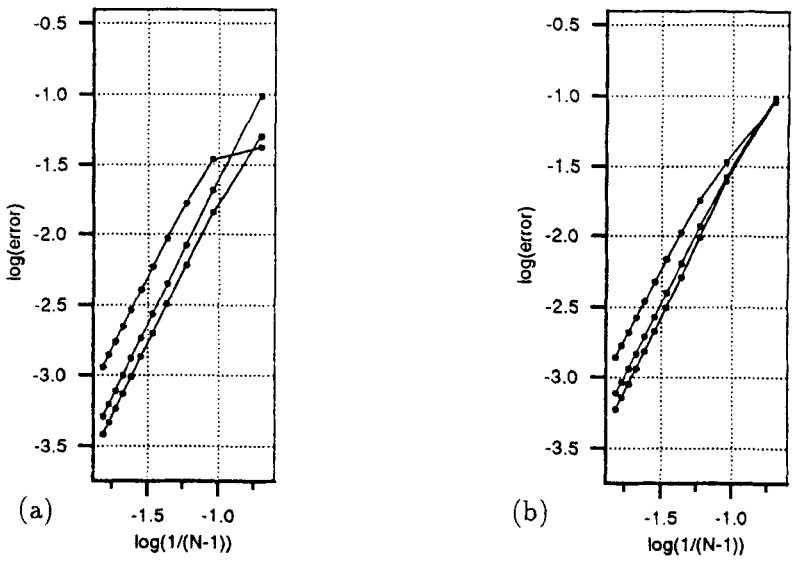

Figure 16. Convergence for the helical test problem of (a) planar and (b) upwind triangulated methods on successively stretched parallelepiped meshes; $\mu=0, 2{\cdot}5, 5$

residuals and boundary conditons is thus wellposed and may be efficiently inverted using a Gauss–Seidel procedure ordered to follow the flow direction.

For the same reason given in Section 4.1 Q was chosen as the smooth function

$$Q(u, v) = \exp\{-[u\cos(v) - \tfrac{1}{4}]^2 - [u\sin(v) + \tfrac{1}{4}]^2\}.$$

Throughout these numerical results $\boldsymbol{a}$ was fixed at $(3, 2, 1)^T$; since the mesh was sheared along $\boldsymbol{a}$, this is equivalent to an (r, s, t) of (3, 2, 0). The data given on the plane $z = 0$ were rotated through 2π, i.e. $\omega = \pi$.

Figure 16 compares the convergence behaviour of the planar and upwind triangulated methods on stretched parallelepiped meshes. As for the constant coefficient test problem of Figure 10, both methods are clearly second-order-accurate. The planar method is superior on an unstretched mesh, but this superiority is lost for $\mu = 5$. Figure 17 shows the effect of randomizing the meshes. These results demonstrate the remarkable accuracy of the upwind triangulated method compared to the planar method on severely distorted grids. This effect is even more striking for this helical test problem than for the constant coefficient case of Figure 11. Whilst the upwind triangulated method can maintain an accurate solution up to 40% randomness, the planar method fails even for 20%. These results are further emphasized by Figure 18, which shows the convergence behaviour on successively randomized stretched grids. A qualitative illustration of the accuracy of the two methods is provided by Figure 19, which shows a contour plot of the solution on the plane $z = 0$ together with the approximate solutions obtained on the plane $z = 2$ by each method.

5. CONCLUSIONS

It has been shown that there is no unique generalization of the cell vertex method to three dimensions but rather a one-parameter family of methods, all of which have second-order

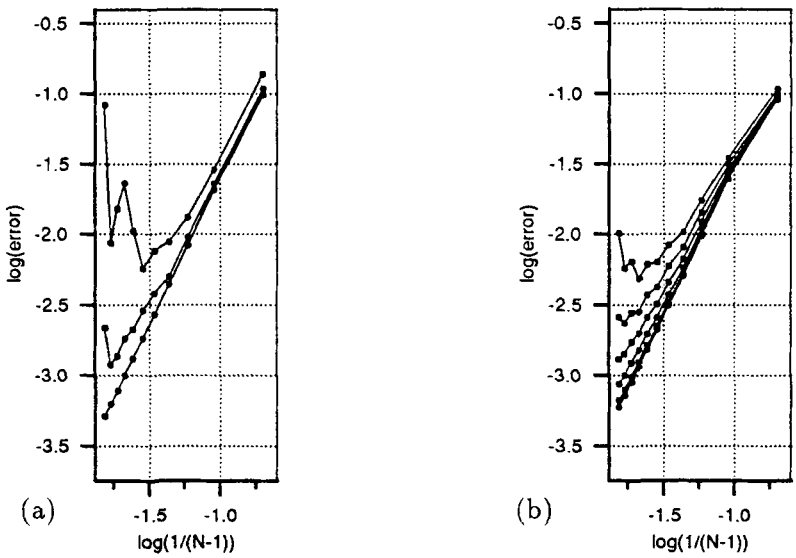

Figure 17. Convergence for the helical test problem of (a) planar and (b) upwind triangulated methods on successively randomized meshes; $\mu = 0$, with η increasing from zero in increments of 10

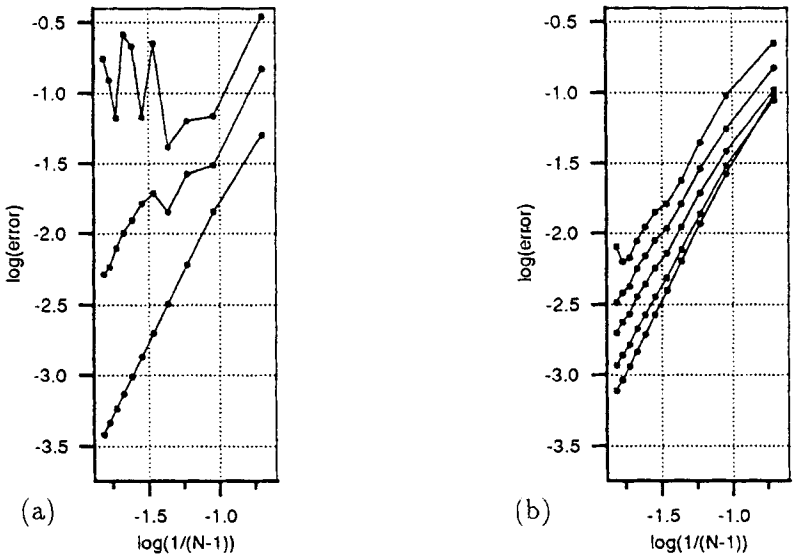

Figure 18. Convergence for the helical test problem of (a) planar and (b) upwind triangulated methods on successively randomized stretched meshes; $\mu = 2{\cdot}5$, with η increasing from zero in increments of 10

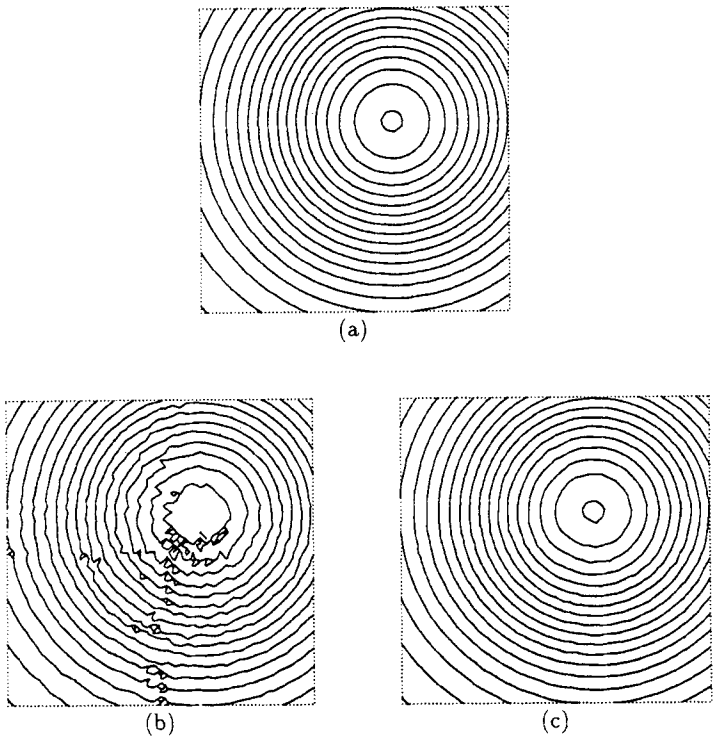

Figure 19. Contours of (a) Dirichlet data on the plane $z = 0$, (b) the numerical representation of this after being rotated through 2π using the planar method and (c) using the upwind triangulated method; $N = 47$, $\mu = 20\%$

truncation errors on parallelepiped control volumes. Finite volume discretizations with triangulated faces have been derived and recognized as members of this family. The greater flexibility available in three dimensions allows a method to be selected with advantageous spectral properties. Since these methods put greater bias on particular coefficients of the stencil, they may be interpreted as upwind schemes. Numerical experiments have shown that as well as having better spectral properties, upwind triangulated methods are also more accurate on distorted meshes than the more commonly used planar method. However, if the triangulation does not take account of the flow direction, an unstable method may result and second-order accuracy is not achieved.

The flexibility available in triangulating control volumes has been demonstrated via the imposition of a variable coefficient helical flow field. For an upwind triangulation scheme, second-order global accuracy was observed up to a high degree of mesh distortion. This was not the case for the planar method.

As in one and two dimensions, there exist compact and accurate cell vertex finite volume discretizations, which are thought to be ideal for systems of conservation laws.

ACKNOWLEDGEMENTS

This work was supported by the Science and Engineering Research Council (G.J.S.) and British Aerospace (P.I.C.)

REFERENCES

1. P. L. Roe, 'The influence of mesh quality on solution accuracy', *Preprint*, Cranfield Institute of Technology, 1987.
2. K. W. Morton and M. F. Paisley, 'A finite volume scheme with shock fitting for the steady Euler equations', *J. Comput. Phys.*, **80**, 168–203 (1989).
3. M. Giles, 'Accuracy of node based solutions on irregular meshes', *Proc. ICNMFD 11*, Springer, New York, 1988, pp. 273–277.
4. E. Süli, 'Finite volume methods on distorted mashes: stability accuracy, adaptivity', *Oxford University Computing Laboratory Report 89/6*, 1989.
5. K. W. Morton and M. A. Rudgyard, 'Shock recovery and the cell vertex scheme for the steady Euler equations', *Proc. ICNMFD 11*, Springer, New York, 1989, pp. 424–428.
6. C. Koeck, 'Computation of three dimensional flows using the Euler equations and a multiple-grid scheme', *Int. j. numer. methods fluids*, **5**, 483–500 (1985).
7. D. J. Salmond, 'A cell vertex multigrid scheme for solution of the Euler equations for transonic flow past a wing', *Proc. ICNMFD 10, Springer Lecture Notes in Physics, Vol. 264*, Springer, New York, 1986.
8. K. W. Morton and M. A. Rudgyard, 'Finite volume methods with explicit shock representation', to appear *Conf. on Computational Aeronautical Fluid Dynamics*, Antibes, 1989.
9. K. W. Morton, 'Finite volume methods and their analysis', *Proc. Conf. on the Mathematics of Finite Elements and Applications*, Academic Press, 1991, pp. 189–214.
10. P. I. Crumpton, J. A. Mackenzie, K. W. Morton, M. A. Rudgyard and G. J. Shaw, 'Cell vertex multigrid methods for the compressible Navier–Stokes equations', *Proc. ICNMFD 12*, 1990, Springer-Verlag, Oxford, pp. 243–247.